Two-dimensional streaming flows driven by sessile semicylindrical microbubbles

Bhargav Rallabandi, Cheng Wang and Sascha Hilgenfeldt†

Department of Mechanical Science and Engineering, University of Illinois at Urbana-Champaign,
1206 West Green Street, Urbana, IL 61801, USA

Steady streaming flow from oscillating sessile bubbles at walls is the centrepiece of many microstreaming experiments. A complete asymptotic theory of the flow is developed, requiring only the oscillatory driving frequency and material parameters as input, and properly accounting for bubble and wall boundary conditions. It is shown that mixed-mode streaming of neighbouring bubble oscillation modes is responsible for the robustness of the generic 'fountain' vortex pair flow pattern, and that the pattern reverses for high frequencies when wall-induced streaming becomes dominant. The far-field flow and its dependence on control parameters are in agreement with experimental data and can be understood considering just a few asymptotic coefficients.

Key words: acoustics, bubble dynamics, microfluidics

1. Introduction

Steady streaming is the name given to flow phenomena resulting from a time average over oscillatory fluid motion, arising in a variety of scientific and engineering applications (see, e.g., Lighthill 1978; Riley 2001; Marmottant & Hilgenfeldt 2003; Lutz, Chen & Schwartz 2006; Wang, Rallabandi & Hilgenfeldt 2013*a*). We focus here on streaming induced by oscillatory boundary motion, a subject that has long been studied in the context of translational oscillations of objects and resulting transport phenomena (Raney, Corelli & Westervelt 1954; Riley 1966; Lutz *et al.* 2006). Large oscillation amplitude is a desirable feature to ensure strong streaming flows (streaming flow speed being quadratically dependent on the amplitude), which has led to recent interest in streaming induced by the oscillation of bubbles (Marmottant & Hilgenfeldt 2003; Ahmed *et al.* 2009; Wang, Jalikop & Hilgenfeldt 2011). While translational bubble oscillations (without volume change) lead to weak streaming (Davidson & Riley 1971; Longuet-Higgins 1998), the presence of volume oscillations causes much stronger flows that have been demonstrated as efficient tools for transport (Wang, Jalikop & Hilgenfeldt 2012), shear force actuation (Marmottant & Hilgenfeldt 2003), particle trapping and size sorting (Patel, Tovar & Lee 2012; Wang *et al.* 2011), or micromixing (Ahmed *et al.* 2009; Wang *et al.* 2013*a*) applications. In practically relevant situations, ultrasound-driven bubbles are sessile at walls in microfluidic devices, and the generic streaming flow pattern consists of a vortex system above

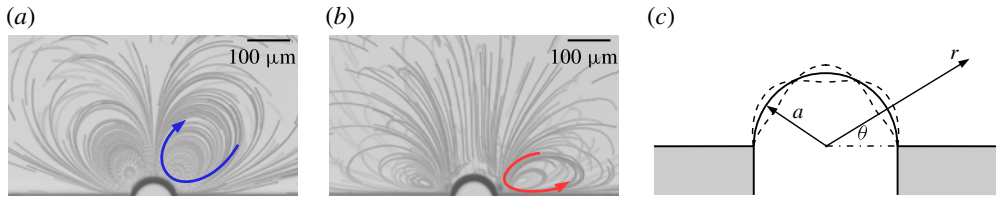† Email address for correspondence: sascha@illinois.edu

FIGURE 1. (Colour online) (*a*,*b*) Pathlines of the steady streaming around an oscillating bubble of radius $a = 45 \, \mu m$ (bottom centre), visualized by neutrally buoyant tracer particles of 1 μm radius. Arrows indicate the orientation of the flow at (*a*) $f = 20$ kHz (fountain) and (*b*) $f = 84$ kHz (antifountain); (*c*) geometry of the problem showing the coordinate system. Dashed lines in (*c*) indicate the position of the interface at two instants of time.

the bubble, expelling liquid upwards along the bubble's symmetry axis ('fountain' streaming flow, see figure 1*a*).

A systematic theoretical analysis of such sessile bubble streaming flows has, however, been missing. While some direct numerical simulations of specific cases exist (Liu *et al.* 2002), asymptotic theories (Longuet-Higgins 1998; Marmottant & Hilgenfeldt 2004; Liu & Wu 2009; Doinikov & Bouakaz 2010) have neglected one or several of the salient features that make the problem unique and different from other streaming situations: (i) the bubble oscillation occurs not in bulk, but the fluid is a half-space defined by the wall; (ii) the bubble is attached to the wall by contact lines; (iii) two different oscillatory boundary layers exist at the wall (no slip) and around the bubble (no stress); and (iv) the bubble's free surface is capable of oscillations in various modes. In this paper, we derive a streaming solution taking into account all of these factors. The theory shows that several oscillation modes can be involved in the generation of the typical streaming flow pattern and explains why the 'fountain' is generically observed over a wide range of ultrasound driving frequencies. It also demonstrates that for large enough frequencies, the fountain flow is altered and eventually replaced by a vortex pattern of reversed orientation ('antifountain', figure 1*b*). These findings are in good agreement with experiment and constitute a complete derivation of sessile microbubble streaming flow with only the (dimensionless) driving frequency and a damping coefficient as input parameters.

2. Two-dimensional bubble streaming theory

We consider the steady flow induced by a harmonically oscillating semicylindrical bubble (of semicircular cross-section) attached to a rigid wall via stationary contact lines as shown in figure 1(*c*). The bubble has a rest radius *a* and its surface oscillates with angular frequency $\omega = 2\pi f$ and characteristic amplitude ϵa, where $\epsilon \ll 1$, driving the fluid around it at the characteristic oscillatory velocity $U_0 = \epsilon a \omega$. As is typical of several microfluidics applications (Liu *et al.* 2002; Marmottant & Hilgenfeldt 2003; Ahmed *et al.* 2009), oscillations of the interface in our experiments are set up by an externally applied acoustic field ($f \sim 1$–100 kHz), whose wavelength (~ 1 cm–1 m) is much greater than the radius of the bubble ($a \approx 50 \, \mu m$), and may therefore be considered as spatially uniform in practice.

We are interested primarily in the two-dimensional flow excited by such a bubble, which is both useful and accurate as an approximation in the context of flows in microfluidic devices (Wang *et al.* 2011, 2012). In particular, axial oscillations of the bubble are only weakly excited due to much stronger damping, and drive three-

dimensional flows which decay much more rapidly away from the bubble, so that the dominant oscillations of the interface are in the plane perpendicular to the bubble axis (Wang *et al.* 2013*a*). In our experiments, the bubble has an axial dimension $D = 100\,\mu\text{m} \sim 2a$, which is also the wavelength of the lowest permitted axial mode. Since oscillation modes of small wavelengths are more strongly damped, axial modes are expected to become comparably excited only for larger values of D, as shown by Wang *et al.* (2013*a*).

In a polar coordinate system (r, θ) coaxial with the axis of the bubble, with the rigid walls to which the bubble is attached at $\theta = 0$ and $\theta = \pi$, the bubble surface is described in units of a as

$$R(\theta, t) = 1 - i\epsilon\zeta(\theta)e^{it} \tag{2.1}$$

where $\zeta(\theta)$ is $O(1)$ and only the real part of any complex quantity is physically meaningful. Using characteristic length, time and velocity scales a, ω^{-1} and U_0, respectively, we define a dimensionless stream function ψ, related to radial and azimuthal velocity components by $u = r^{-1}\partial_\theta\psi$ and $v = -\partial_r\psi$, respectively. The planar flow is governed by the Navier–Stokes equations in two dimensions,

$$\frac{\partial \nabla^2\psi}{\partial t} - \frac{\epsilon}{r}\frac{\partial(\psi, \nabla^2\psi)}{\partial(r, \theta)} = \frac{\delta^2}{2}\nabla^4\psi, \tag{2.2}$$

where $\partial(f, g)/\partial(x, y)$ denotes the Jacobian determinant and $\delta \equiv \sqrt{2\nu/(a^2\omega)}$ is the dimensionless oscillatory boundary-layer thickness, assumed small compared with the radius of the bubble ($\delta \ll 1$), a condition practically realized in many microfluidics applications (e.g. Marmottant & Hilgenfeldt 2004; Wang *et al.* 2011; Patel *et al.* 2012). The motion of the interior gas will be neglected, as its density and dynamic viscosity are negligible compared with those of the exterior liquid.

As is standard practice in analytical treatments of streaming (Nyborg 1958; Riley 1967; Longuet-Higgins 1998; Riley 2001), we develop an asymptotic solution in powers of ϵ: $\psi = \psi_0 + \epsilon\psi_1 + O(\epsilon^2)$. The leading-order stream function ψ_0 is then governed by

$$\left(\frac{2}{\delta^2}\frac{\partial}{\partial t} - \nabla^2\right)\nabla^2\psi_0 = 0, \tag{2.3}$$

along with effective boundary conditions (kinematic and zero tangential stress) at the mean position of the interface

$$\left.\begin{array}{ll}
\dfrac{1}{r}\dfrac{\partial\psi_0}{\partial\theta} = \zeta e^{it} & \text{on } r = 1, \\[3mm]
\dfrac{\partial^2\psi_0}{\partial r^2} - \dfrac{1}{r}\dfrac{\partial\psi_0}{\partial r} - \dfrac{1}{r^2}\dfrac{\partial^2\psi_0}{\partial\theta^2} = 0 & \text{on } r = 1,
\end{array}\right\} \tag{2.4}$$

in addition to no-slip conditions at the walls,

$$\frac{\partial\psi_0}{\partial r} = \frac{1}{r}\frac{\partial\psi_0}{\partial\theta} = 0 \quad \text{on } \theta = 0 \text{ and } \theta = \pi. \tag{2.5}$$

In general, ψ_1 consists of both oscillatory and steady components, of which we are interested primarily in the latter, here denoted by the time average $\langle\psi_1\rangle$. This constitutes the Eulerian mean flow and is governed by an inhomogeneous Stokes

equation

$$\nabla^4 \langle \psi_1 \rangle = -\frac{2}{\delta^2} \left\langle \frac{1}{r} \frac{\partial (\psi_0, \nabla^2 \psi_0)}{\partial (r, \theta)} \right\rangle, \tag{2.6}$$

provided that the streaming Reynolds number $Re_s \equiv \epsilon^2/\delta^2 \ll 1$ (see e.g. Stuart 1966). In practice, the steady motion of individual fluid elements is of greater relevance; it is evaluated by augmenting the Eulerian stream function with a Stokes drift term ψ_d, defined as (Raney *et al.* 1954)

$$\psi_d = \left\langle \frac{1}{r} \frac{\partial \psi_0}{\partial \theta} \int -\frac{\partial \psi_0}{\partial r} \mathrm{d}t \right\rangle. \tag{2.7}$$

In analogy to the work of Longuet-Higgins (1998), but more generally, it can be shown (appendix A) that for periodic interfacial motion with arbitrary $\zeta(\theta)$, a consistent expansion of the no-penetration and no-stress boundary conditions in ϵ yields particularly simple expressions for the first-order time-averaged terms when expressed in the Lagrangian stream function $\Psi = \langle \psi_1 \rangle + \psi_d$. In particular, both radial velocity and tangential stress due to Ψ vanish at the mean position of the interface, i.e.

$$\left. \begin{aligned} \frac{1}{r} \frac{\partial \Psi}{\partial \theta} &= 0 \quad \text{on } r = 1, \\ \frac{\partial^2 \Psi}{\partial r^2} - \frac{1}{r} \frac{\partial \Psi}{\partial r} - \frac{1}{r^2} \frac{\partial^2 \Psi}{\partial \theta^2} &= 0 \quad \text{on } r = 1, \end{aligned} \right\} \tag{2.8}$$

in addition to no-slip conditions at the walls, given by

$$\frac{\partial \Psi}{\partial r} = 0, \quad \text{on } \theta = 0 \text{ and } \theta = \pi, \tag{2.9a}$$

$$\frac{1}{r} \frac{\partial \Psi}{\partial \theta} = 0, \quad \text{on } \theta = 0 \text{ and } \theta = \pi. \tag{2.9b}$$

We note that in typical microfluidics applications, the presence of surfactants may in general modify the no-stress condition at the interface. However, a remobilization of the interface occurs if the concentration of surfactant exceeds its critical micelle concentration (CMC), and if the rate of micellization is faster than the rate of convective transport along the interface (Stebe & Maldarelli 1994; Wang, Papageorgiou & Maldarelli 1999). In our experiments, we use the polyexthoxylated (PEO) surfactant Tween 20 (Stebe & Maldarelli 1994) at 1 % w/w in solution (far greater than its CMC). In addition, the relaxation times of typical PEO surfactants ($\sim 100\,\mu\text{s}$) (Brown, Pu & Rymdén 1988) are much shorter than characteristic time scales of mass transport along the interface by the streaming flow (1–2 ms). This suggests that the surfactants do not retard the fluid motion near the interface, and a no-stress condition at the interface is indeed applicable. This is further validated by experimental measurements that indicate no drop in tangential velocity near the interface (e.g. figure 3c), and also by additional experiments with oscillatory channel flow over bubbles that show flow patterns that differ greatly from those induced by oscillating cylinders (see, e.g., Lutz, Chen & Schwartz 2005).

3. General solutions to the Lagrangian mean flow

From the above, we see that the streaming flow follows as a second-order effect from the first-order oscillatory flow, which is in turn a function of the dynamics

of the interface as a response to the driving frequency. While the system of equations (2.3)–(2.9a) is not amenable to a general analytical solution for ψ_0 and ψ_1, an approximate solution using matched asymptotic expansions can be developed for $\delta \ll 1$.

We build here on our own previous results on the bubble interface dynamics (Wang *et al.* 2013a) as well as on long-standing results on the streaming flow near a rigid no-slip wall (Longuet-Higgins 1953; Nyborg 1958; Riley 2001). For $\delta \ll 1$, Longuet-Higgins (1953) showed that for an imposed oscillatory slip velocity $u_s(r)e^{it}$, the steady Lagrangian slip velocity that persists at the outer edge of the wall boundary layer is given by

$$U_s = -\frac{3 - 5i}{4} u_s^* \frac{du_s}{dr}, \tag{3.1}$$

where u_s^* is the complex conjugate of u_s.

We now develop a formalism to evaluate the Lagrangian streaming outside the wall boundary layer, which must satisfy both the boundary conditions at the bubble (2.8) and support the steady slip velocity U_s at the wall, in order to match the steady wall boundary layer solution. As shown by Wang *et al.* (2013a), the solution to the oscillatory flow problem (2.3)–(2.5), valid outside the wall boundary layer ($r\theta \gg \delta$) is, to leading order in δ,

$$\psi_{0b}(r, \theta) = \sum_{n=0}^{\infty} \psi_0^n(r, \theta) = \sum_{n=0}^{\infty} A_n \left(\frac{c_{2n}}{r^{2n}} + d_{2n} K_{2n}(\alpha r) \right) \sin 2n\theta \, e^{it}, \tag{3.2}$$

where A_n is in general complex, $\alpha \equiv (1 + i)/\delta$,

$$c_k = \frac{1}{k} - d_k K_k(\alpha) \quad \text{and} \quad d_k = -\frac{2(k + 1)}{\alpha^2 K_{k-2}(\alpha) + 2k\alpha K_{k-1}(\alpha)}. \tag{3.3}$$

The oscillatory slip velocity amplitude at the edge of the wall boundary layer is then

$$u_s(r) = \sum_{n=0}^{\infty} \frac{A_n}{r^{2n+1}} + O(\delta^2), \tag{3.4}$$

and ultimately determines the steady slip velocity U_s via (3.1).

Since ψ_{0b} represents the oscillatory flow outside the wall boundary layer, it may be used in place of the full oscillatory stream function ψ_0 in (2.6) and (2.7) to obtain the Lagrangian mean flow function in this region. Taking Ψ to henceforth denote the Lagrangian mean stream function *outside* the wall boundary layer, equation (2.9a) is replaced to leading order by the slip condition

$$\frac{1}{r} \frac{\partial \Psi}{\partial \theta} = U_s \quad \text{on } \theta = 0 \text{ and } \theta = \pi, \tag{3.5}$$

to properly match the steady Lagrangian wall boundary-layer solution, while retaining the boundary conditions (2.8) and (2.9a). The flow resulting from Ψ can be directly compared with experimental trajectory data from passive tracer particles.

The analysis is aided by the explicit decomposition of $\langle \psi_1 \rangle$ into a homogeneous solution ψ_{hom} and a particular solution ψ_p. As a general feature of streaming flows with $\delta \ll 1$, the particular solution of (2.6) decays exponentially over a scale of δ away from the boundaries of the domain (Longuet-Higgins 1953). Specifically, while the particular solution of (2.6) with (3.2) can be written in closed form using classical

techniques (see e.g. Raney *et al.* 1954), it is more appropriate to retain the asymptotic behaviour of ψ_p only, in order to remain consistent with the boundary-layer treatment of the flow. To determine ψ_p outside the wall boundary layer, both (2.6) and (3.2) are expanded in powers of δ, using a bubble boundary-layer coordinate $\eta \equiv (r-1)/\delta$. This yields a linear fourth-order ordinary differential equation which is solved for $\psi_p(\eta)$. On the other hand, the Stokes drift (2.7) evaluated with (3.2) exhibits slower algebraic decay that persists in the bulk of the fluid, in addition to exponentially decaying terms. Note also that in the evaluation of time averages of products of oscillatory quantities in (2.6) and (2.7), we use the identity $\langle \mathrm{Re}(p\,\mathrm{e}^{\mathrm{i}t})\,\mathrm{Re}(q\,\mathrm{e}^{\mathrm{i}t}) \rangle = \mathrm{Re}(p\,q^*)/2$, valid for any complex time-independent quantities p and q.

Using (14), (15) and (25) of the analysis of Wang *et al.* (2013*a*), it can be shown that the coefficients A_n are to $O(\delta^3)$ equal to the Fourier cosine coefficients $\zeta_n = a_n \mathrm{e}^{\mathrm{i}\phi_n}$ of the interface deformation $\zeta(\theta)$, where a_n is a positive mode amplitude and ϕ_n is a real phase angle. Note that in Wang *et al.* (2013*a*) these amplitudes and phases were derived directly from the physical parameters of the bubble oscillator (ω, a, ν) and can be taken as inputs for the calculation below. In the following, we will normalize the a_n by the volume mode amplitude a_0, defining $\bar{a}_n \equiv a_n/a_0$, and use relative phase angles $\phi_{m,n} \equiv \phi_m - \phi_n$. In order to determine the streaming flow pattern, we set $a_0 = 1$ without loss of generality, as it can be absorbed in the amplitude scale ϵ.

While the individual expressions for ψ_p and ψ_d are rather involved, their combined contribution to the flow field is simpler, and is more favourably written by the rearrangement $\psi_p + \psi_d = \Psi^+ + \Psi^-$, where

$$\Psi^\pm = \sum_{m>n}^{\infty} \sum_{n=0}^{\infty} \Psi_{m,n}^\pm \sin 2(m \pm n)\theta, \tag{3.6}$$

with

$$\left. \begin{aligned} \Psi_{m,n}^+ &= \frac{\bar{a}_m \bar{a}_n}{1+\delta_{mn}} 2\delta^2 (2m+1)(2n+1) \cos\phi_{m,n}\, \mathrm{e}^{-(1+\mathrm{i})\eta} \quad \text{and} \\ \Psi_{m,n}^- &= \bar{a}_m \bar{a}_n \left\{ \frac{1}{2r^{2(m+n+1)}} + 2\mathrm{i}\,\delta^2 (2m+1)(2n+1)\, \mathrm{e}^{-(1+\mathrm{i})\eta} \right\} \sin\phi_{m,n}, \end{aligned} \right\} \tag{3.7}$$

so that the Lagrangian stream function is given by $\Psi = \psi_{hom} + \Psi^+ + \Psi^-$. Note that algebraically decaying terms in (3.7) are due entirely to the Stokes drift and appear only in Ψ^-.

The homogeneous Stokes solutions ψ_{hom} must be chosen so that the Lagrangian stream function Ψ satisfies the boundary conditions (2.8) and provides the steady slip U_s at the edge of the wall boundary layer. We also note that the $O(\delta^2)$ boundary layer terms in (3.7) do not contribute to the velocity field at leading order, but can in general make a leading-order contribution to the tangential stress at the bubble. However, we find that to this leading order, the real part of the tangential stress at the interface due to Ψ^+ vanishes identically, which allows us to neglect Ψ^+ altogether in further calculations. Thus, Ψ^- carries the sum total of contributions to the streaming that arise directly from the specific oscillations of the bubble itself, independent of the presence of the wall. It is also worth noting that all Ψ^- terms arise from the coupling of distinct oscillation modes (*mixed-mode streaming*), rather than from interaction of a mode with itself.

The slip condition at the edge of the wall boundary layer, evaluated using (3.1) and (3.4), is accommodated by expressing ψ_{hom} as a sum of elementary Stokes solutions

that are either no-slip solutions (zero velocity at the wall) or slip solutions (zero normal velocity at the wall). The Lagrangian stream function then takes the form

$$\Psi = \sum_{k=1}^{\infty} \frac{e_k}{r^{2k-1}} \{\cos(2k-1)\theta - \cos(2k+1)\theta\}$$

$$+ \sum_{k=1}^{\infty} \frac{f_k}{r^{2k}} \left\{ \frac{1}{2k} \sin 2k\theta - \frac{1}{2(k+1)} \sin 2(k+1)\theta \right\} + \psi_s + \Psi^-, \qquad (3.8)$$

where e_k and f_k are coefficients of two series of no-slip Stokes solutions, and ψ_s represents homogeneous slip solutions of (2.6). The slip condition on the Lagrangian mean flow (3.5) is then simply a condition on ψ_s, written explicitly in terms of normalized mode amplitudes and relative phase angles between modes as

$$\frac{1}{r} \frac{\partial \psi_s}{\partial \theta} = \sum_{m \geqslant n}^{\infty} \sum_{n=0}^{\infty} \frac{\bar{a}_m \bar{a}_n}{r^{2m+2n+3}} \frac{3}{2} \left\{ \frac{(m+n+1)\cos\phi_{m,n}}{1+\delta_{mn}} + (m-n)\sin\phi_{m,n} \right\}$$

$$\text{on } \theta = 0 \text{ and } \theta = \pi. \qquad (3.9)$$

Since ψ_s may be any fundamental slip solution of (2.6) that satisfies (3.9), we choose it to be a harmonic function without loss of generality, to obtain

$$\psi_s = \sum_{m \geqslant n}^{\infty} \sum_{n=0}^{\infty} \frac{\bar{a}_m \bar{a}_n}{r^{2(m+n+1)}} \frac{3}{4} \left\{ \frac{\cos\phi_{m,n}}{1+\delta_{mn}} + \frac{(m-n)\sin\phi_{m,n}}{m+n+1} \right\} \sin 2(m+n+1)\theta. \quad (3.10)$$

With this definition of ψ_s, the Lagrangian stream function Ψ defined by (3.8) spans the entire family of solutions satisfying (3.5). The boundary conditions (2.8) at the surface of the bubble, applied to the Lagrangian steady stream function in (3.8), lead to two equations valid for $0 < \theta < \pi$, which when written in an orthogonal Fourier basis, yield a system of linear algebraic equations in e_k and f_k,

$$\left. \begin{array}{l} f_k - f_{k-1} - \dfrac{128}{\pi} \displaystyle\sum_{j=1}^{\infty} \dfrac{jk^2 e_j}{16j^4 + 16k^4 - 32j^2k^2 - 8j^2 - 8k^2 + 1} = g_k, \\[4mm] (k+1)f_k - (k-1)f_{k-1} - \dfrac{32}{\pi} \displaystyle\sum_{j=1}^{\infty} \dfrac{jk(2j+1)(2j-1)e_j}{16j^4 + 16k^4 - 32j^2k^2 - 8j^2 - 8k^2 + 1} = \dfrac{h_k}{2}, \end{array} \right\} \quad (3.11)$$

valid for all positive integers k, where it is understood that e_k and f_k are identically zero for $k \leqslant 0$. Here, g_k and h_k are the negatives of Fourier sine and cosine components, respectively, of the contribution of $\hat{\psi} \equiv \psi_s + \Psi^-$ to normal velocity and tangential stress, defined as

$$\left. \begin{array}{l} g_k \equiv -\dfrac{2}{\pi} \displaystyle\int_0^{\pi} \dfrac{1}{r} \dfrac{\partial\hat{\psi}}{\partial\theta} \cos 2k\theta \, \mathrm{d}\theta \quad \text{on } r = 1, \\[4mm] h_k \equiv -\dfrac{2}{\pi} \displaystyle\int_0^{\pi} \left(\dfrac{\partial^2\hat{\psi}}{\partial r^2} - \dfrac{1}{r} \dfrac{\partial\hat{\psi}}{\partial r} \right) \sin 2k\theta \, \mathrm{d}\theta \quad \text{on } r = 1, \end{array} \right\} \quad (3.12)$$

terms of $O(\delta)$ and higher being neglected in both g_k and h_k. Note that definitions for g_k and h_k follow directly from (2.8), with the simplification that the no-penetration condition allows us to drop the azimuthal derivatives in the formula for the stress at the interface. The linear system (3.11) after some manipulation yields analytical

expressions for e_k and f_k,

$$
\left.\begin{aligned}
f_k &= \frac{1}{4}\left((k+1)h_k - k\,h_{k+1}\right) - \frac{1}{2}\left((k+1)(k-1)g_k - k(k+2)g_{k+1}\right), \\
e_k &= \frac{4}{\pi}\sum_{j=1}^{k}\sum_{i=1}^{\infty}\frac{f_i - f_{i-1} - g_i}{(2j+2i-1)(2j-2i-1)}.
\end{aligned}\right\}
\tag{3.13}
$$

The normalized amplitudes $\bar{a}_n$ and relative phases $\phi_{m,n}$ may either be extracted directly from shape oscillations of the bubble, or via a theoretical calculation of the dynamics of bubble oscillation (Wang *et al.* 2013*a*), which enables the evaluation of the Lagrangian mean flow up to the scaling factor ϵ^2 (determined experimentally by the amplitude of the driving ultrasound). The bubble dynamics itself is a function of two dimensionless parameters: the driving frequency normalized by the frequency scale governing surface mode excitation (λ), and a viscous damping constant (γ), defined as $\lambda \equiv \omega(\rho a^3/\Gamma)^{1/2}$ and $\gamma \equiv \lambda\delta^2/2$. Here, Γ is the surface tension and ρ is the density of the liquid (Wang *et al.* 2013*a*). In practically relevant situations, the damping is small ($\gamma \ll 1$).

4. Results and discussion

We evaluate the steady streaming using mode amplitudes and phases both from experimental measurements and dynamical calculations, which are in good agreement with each other. In practice, the infinite sums in (3.6)–(3.8) can be truncated at a finite N to good accuracy; for the theoretical results reported here, we take $N = 3$, which is also the number of surface modes that have been identified quantitatively in experiment. While higher modes may be excited in experiment, their amplitudes are smaller due to stronger damping and play a negligible role in determining the shape of the interface; we will justify this more precisely in the next paragraph. We find that the steady flow pattern is characterized by closed vortical flow lines. Over a wide range of frequencies and damping parameters, the velocity field in the bulk of the fluid is inward close to the wall, and radially outwards near the pole of the bubble in a '*fountain*' vortex pair, precisely the generically observed flow pattern of bubble microstreaming devices, see figures 1(*a*) and 2(*a*,*b*). A tiny secondary vortex pair near the pole of the bubble is also typically predicted and observed in experiment (figure 2*a*,*b*).

A quantitative comparison between experiment and theory in terms of non-dimensional variables requires the determination of the value of ϵ in experiment, which is identified with the amplitude a_0 of volume oscillations and sets the velocity scale in the system. Over a cycle of its oscillation, the interface sweeps a range of radial coordinates $R(\theta, t)$ as defined in (2.1), over an interval of size $\Delta R(\theta)$, cf. the dashed lines in figure 1(*c*). From experimental images, we determine the maximal value ΔR_m of $\Delta R(\theta)$. The theory of Wang *et al.* (2013*a*) predicts the normalized mode amplitudes $\bar{a}_n$ and relative phases $\phi_{n,0}$, and therefore also predicts the ratio $\Delta R_m/(2\epsilon)$. Owing to the dominance of the monopole amplitude (ϵ) over surface mode amplitudes, this numerical factor is of $O(1)$ over the entire range of frequencies of interest. Furthermore, the precise value of the ratio $\Delta R_m/(2\epsilon)$ depends only very weakly on the number of modes N taken into account as long as $N \geqslant 3$, and agrees well with the value obtained by using experimentally measured amplitudes and phases. This determines ϵ and therefore the interface shape $R(\theta, t)$ to good accuracy using the experimental images, and is further justification for the truncation at $N = 3$.
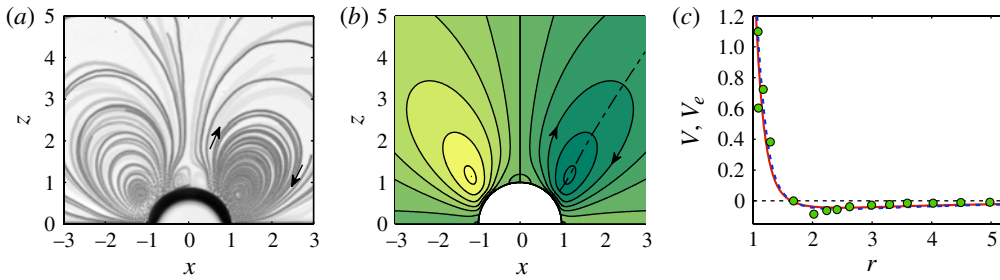
FIGURE 2. (Colour online) Comparison of fountain flows in experiment and theory. (*a*) Experimental streamlines of Lagrangian steady flow at $f = 26.7$ kHz; (*b*) computed streaming pattern at the corresponding dimensionless frequency $\lambda = 9.32$, using amplitudes and phases from the analysis of Wang *et al.* (2013*a*). The agreement is representative of the entire regime of fountain flow patterns. (*c*) Steady Lagrangian azimuthal velocity v along lines of zero radial velocity (indicated as dot-dashed line in *b*), as a function of radial distance r: direct measurements from an experimental run at $f = 26.7$ kHz (○), computed from bubble oscillation amplitudes obtained from interface tracking experiments (Wang *et al.* 2013*a*) of a different run at the same f (– –), and computed from theoretical bubble oscillation amplitudes using only $\lambda = 9.32$ as input (——).

In order to compare not just the flow patterns, but the observed velocities, we evaluate the azimuthal velocity along a line through the points of zero radial velocity in one of the vortices (figure 2*b*). From experimental movies, we determine the monopole amplitude ϵ using the method detailed in the previous paragraph (for figure 2*c*, $\epsilon \approx 0.025$, with a difference of 2.5 % if we take $N = 10$). The azimuthal velocity is then scaled to the streaming velocity scale $U_1 = \epsilon U_0$ to yield V_e. We compare with theoretical calculations of the Lagrangian azimuthal velocity $V = -\partial_r \Psi$ for (i) velocities computed from experimentally measured a_n and $\phi_{m,n}$ values (dashed line in figure 2*c*) and (ii) velocities computed without experimental input directly from the experimental values of λ and γ (solid line). The agreement is very good, and we emphasize that neither the theoretical calculations nor the experimental streaming measurements involve any adjustable parameters. The radial distance of the vortex centre (the zero of the curve in figure 2*c*) is also accurately reproduced, an important quantity for the experimental design of vortex traps (Lutz *et al.* 2006), size sorters (Wang *et al.* 2011, 2012) or micromixers (Wang *et al.* 2013*a*).

The theory also gives insight into the observed reversal of vortex orientation at high frequency (figure 1*b*). At low frequency, it predicts a weak counter-rotating '*antifountain*' vortex pair very close to the wall (figure 3*a*), in order to support the outward slip velocity U_s. As the driving frequency is increased, this near-wall antifountain pair grows in size (figure 3*b*) and eventually (for $\lambda \gtrsim 15$) dominates the entire bulk, confining the fountain vortex pair to small structures near the bubble interface (figure 3*c*). A comparison with experiment at corresponding low (figure 3*d*), intermediate (figure 3*e*) and high driving frequency (figure 1*b*) shows that the salient features of the flowlines are captured. Figure 3(*f*) shows, in addition, that the experimental location of the fountain vortex centre is explained by the theory in very good quantitative agreement throughout the entire range of frequencies, while the position of the antifountain vortex centre is in fair agreement. Antifountain positions are only given for a range of λ where the theory gives unambiguous predictions, i.e. beyond the intermediate-frequency transition range, in which results are strongly
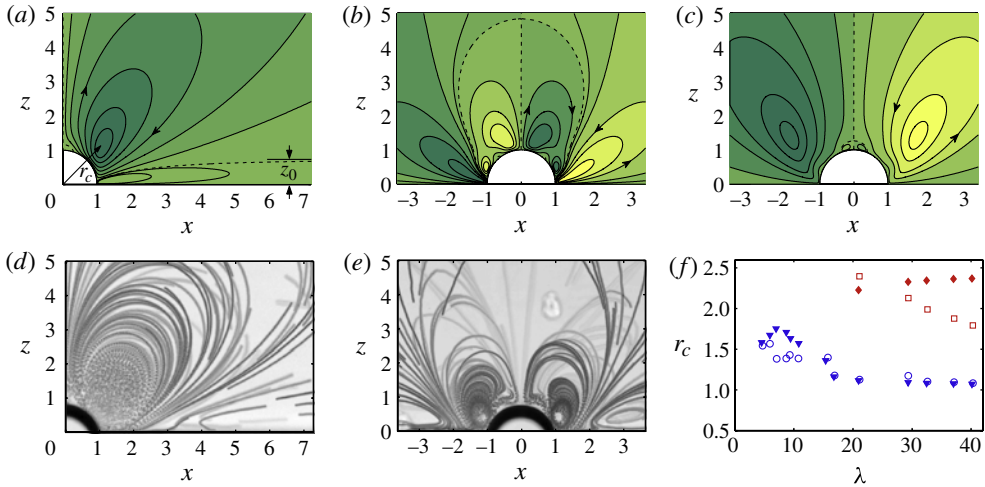
FIGURE 3. (Colour online) Streamlines of Lagrangian steady flow at (*a*) $\lambda = 11.3$, (*b*) $\lambda = 15.4$ and (*c*) $\lambda = 29.3$ indicating the orientation of flow (arrows) and the separatrices between counter-rotating vortical systems (dashed lines). Experimental streakline images at (*d*) $\lambda = 11.3$ and (*e*) $\lambda = 16.9$ visualized using tracers of 1 μm radius; and (*f*) radial location of vortex centres (▼, ○: fountains; ◆, □: antifountains) as a function of dimensionless driving frequency. Filled and open symbols in (*f*) represent theoretically computed and experimentally measured positions, respectively. The experimental streakline image corresponding to (*c*) has been presented in figure 1(*b*).

dependent on higher-order mode details. It should be emphasized, though, that none of the theory predictions relies on any adjustment of free parameters.

This frequency-dependent flow reversal is understood from the far-field behaviour of the stream function. The radially most slowly decaying parts of Ψ take the form

$$\Psi = \frac{3}{8r^2}\left(1 + \frac{16}{3}e_1 r \sin\theta + \frac{8}{3}f_1\sin^2\theta\right)\sin 2\theta + O(r^{-3}), \qquad (4.1)$$

so that the sign of the coefficient e_1 indicates the orientation of the streaming in the bulk, and the far-field velocities decay as r^{-2}. Figure 4(*a*) shows the dependence of e_1 on λ and the agreement of its sign change with the flow reversal: at low frequencies, $e_1 < 0$ and fountain streaming dominates the bulk of the flow. The frequency of flow reversal depends only weakly on the damping coefficient γ. To describe the transition more quantitatively, we obtain the location of the separatrix between the two counter-rotating vortical systems by evaluating the stream function (4.1) to zero. Close to the wall in the far-field ($\sin\theta \to 0$, $r \to \infty$), the vertical height of the separatrix asymptotes to a constant $z_0 \equiv -3/(16e_1)$, indicated in figure 3(*a*). For $e_1 < 0$, the antifountains are thus confined to a narrow strip ($0 < z < z_0$) above the wall, where the stream function assumes the form

$$\Psi \sim \frac{3z}{4r^3}\left(1 - \frac{z}{z_0}\right). \qquad (4.2)$$

Thus, the radial velocity in this region decays more rapidly (r^{-3}) than the velocity in the bulk, explaining the very weak flow observed here.
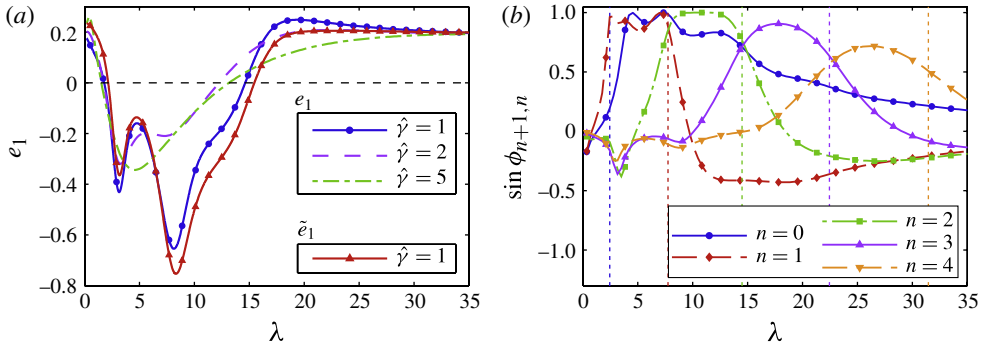
FIGURE 4. (Colour online) (*a*) Coefficient of the most slowly decaying Stokes solution e_1, versus the dimensionless driving frequency λ, for different values of the reduced damping parameter $\hat{\gamma} \equiv \gamma/\gamma_0$, where $\gamma_0 \approx 0.0381$ is the damping constant in the experiments. (*b*) Sine of the relative phase angle $\phi_{n+1,n}$ for various n at $\hat{\gamma} = 1$, indicating a significant contribution in (4.3) primarily between the inviscid surface mode bulk resonance frequencies $\lambda_n = \sqrt{2n(4n^2 - 1)}$ and λ_{n+1} (vertical dashed lines, see Wang *et al.* (2013*a*) for details of the bubble oscillation dynamics).

As the driving frequency is increased, the near-wall antifountains grow in azimuthal extent, and as e_1 becomes positive, the fountain vortices are confined to a finite region near the polar axis of the bubble (cf. figure 3*b*). The separatrix shape can again be understood by setting (4.1) to zero, but now for $\theta = \pi/2$, yielding a positive intersection with the *z*-axis, as our calculations show that $f_1 < 0$ for all λ where $e_1 \geqslant 0$. The fountains ultimately diminish to very small structures at high frequency (figure 3*c*). At the transition point between the fountain and the antifountain regimes where $e_1 = 0$, the far-field becomes dominated by the stronger-decaying velocity components (r^{-3}), as per (4.1). In addition to being weaker, the flow is characterized by two systems of closed streamlines per quadrant, easily understood by the azimuthal dependence of (4.1), setting e_1 to zero. The weakening of the flow near the transition frequency is also present in experiment, where a reduction in the extent of closed stable orbits of tracer particles is observed.

In order to understand the relationship of the far-field streaming with the oscillation modes of the bubble, we first recognize that the no-slip Stokes solution with the slowest radial decay also exhibits the most gradual azimuthal variation. Since the coefficients of the no-slip solutions (e_k and f_k) are ultimately determined by the boundary conditions at the bubble, the far-field no-slip solution depends most strongly on the lowest azimuthal Fourier component of $\hat{\psi}$, i.e. $\sin 2\theta$. This amounts to retaining only g_1 and h_1 in (3.13), yielding an approximation to e_1,

$$e_1 \approx \tilde{e}_1 = \frac{3}{5\pi} \left(1 - \frac{4}{9} \sum_{n=0}^{N-1} \overline{a}_n \overline{a}_{n+1} (4n+1)(4n+5) \sin \phi_{n+1,n} \right), \qquad (4.3)$$

which agrees very closely with the full expression, see figure 4(*a*). The term of (4.3) independent of $\overline{a}_n$ originates from the outward slip along the wall and is driven by volume oscillations of the bubble. In addition to this 'wall-streaming' effect, the far-field flow depends directly on the coupling between pairs of neighbouring oscillation modes n and $n + 1$, whose sign is determined by the sine of the relative phase difference $\phi_{n+1,n}$. For realistic cases of small damping ($\gamma \ll 1$), we find from the

frequency response of the bubble (Wang *et al.* 2013*a*) that for any $n \geqslant 1$ the phase factor $\sin\phi_{n+1,n}$ is of significant size only over a range $\lambda_n \lesssim \lambda \lesssim \lambda_{n+1}$, i.e. between the resonance frequencies of the modes in question (figure 4*b*). Furthermore, within this range the quantity $\sin\phi_{n+1,n}$ is positive, resulting by (4.3) in a negative contribution to e_1. While higher-order surface modes typically have smaller amplitudes (cf. the analysis of Wang *et al.* (2013*a*)), the *n*-dependence in (4.3) ensures that the mixed-mode contribution to e_1 overcomes the wall-streaming contribution for a large range of λ, resulting in $e_1 < 0$ and hence fountain streaming. Equation (4.3) emphasizes the dominance of mixed-mode streaming for sessile microbubbles. We note that while different mixed-mode pairs are dominant at different frequencies, the transitions between mode pairs are smooth and do not show marked changes in the appearance of the flow.

The dominance of coupling between neighbouring modes is understood from general considerations of the oscillation dynamics of the bubble. Every surface mode *n*, driven by volume oscillations of the bubble, exhibits similar amplitude and phase behaviour when driven far from resonance. There is therefore a band of frequencies (of width proportional to γ) around the resonance frequency λ_n, characterized by strong excitation of amplitude $\bar{a}_n$ and significant phase differences with other modes $\phi_{m,n}$. For neighbouring mode pairs $(n, n+1)$, whose resonance frequencies are relatively close together, an overlap of the individual excitation regions results in a range of frequencies between these modes $\lambda_n \lesssim \lambda \lesssim \lambda_{n+1}$ where the amplitudes $\bar{a}_n$, $\bar{a}_{n+1}$ and phase difference $\phi_{n+1,n}$ are substantial. On the other hand, two modes whose resonance frequencies differ greatly will not simultaneously have significant amplitudes, ensuring that non-neighbour mode coupling is only a weaker secondary effect.

This mixed-mode streaming is eventually suppressed at high frequencies, where the mode amplitudes are considerably damped and the phase difference of neighbouring modes is smaller (also note the steady decline of $\sin\phi_{1,0}$ in figure 4). In this limit, the outward slip along the wall takes over as the dominant mechanism for streaming, with $e_1 \to 3/(5\pi)$ and (3.8) simplifying to the analytical expression

$$\Psi = \text{Im}\left\{ \frac{3(w - w^*)}{8\pi\, w^3} \left[\pi + \mathrm{i}w^3 \left\{ 2\left(w^2 + \frac{1}{w^2}\right) + \left(w^3 + \frac{1}{w^3}\right) \ln\frac{w-1}{w+1} \right\} \right] \right\}, \quad (4.4)$$

where $w = r \exp \mathrm{i}\theta$ is a complex variable.

In this wall-dominated high-frequency regime, we find in both theory and experiment that the long axis of the vortex structures appears to point towards the 'corners' where the bubble meets the wall, rather than towards the origin (cf. figure 3*c*). In experiments, however, we find that the vortex centres are located closer to the wall than is predicted by the theory (cf. also the deviations in figure 3*f* at high λ), which may be attributed to out-of-plane streaming flows driven by the walls parallel to the field of view confining the experimental set-up. The influence of these walls is expected to be significant in the large-λ limit, where wall streaming dominates.

It is worth remarking that the slip-driven component of the streaming flow depends primarily on the monopole amplitude and remains essentially constant over the frequency range of interest, in the normalization employed here ($a_0 = 1$); this corresponds to the term in (4.3) independent of $\bar{a}_n$. While the streaming speed measured in experiments can be quite sensitive to the geometry and materials of the experimental set-up (Wang *et al.* 2013*a*), the present approach shows that the mixed-mode streaming contribution to the flow relative to this wall-streaming component diminishes at higher frequency, with the dimensionless velocity in the far-field being

proportional to e_1. Our theory therefore provides a consistent description of the steady flow field under the appropriate normalization, independent of the details of the set-up.

5. Conclusions

This work has completed an asymptotic derivation of two-dimensional microstreaming from sessile bubbles: using only the dimensionless driving frequency λ and damping coefficient γ as inputs, bubble mode oscillation amplitudes and phases can be derived, from which in turn follow the coefficients of the functions governing the streaming flow. For low to moderate λ, the flow is a mixed-mode streaming dominated by neighbouring-mode contributions that, because of their relative phase, lead to the generic fountain streaming pattern observed in experiment. As different pairs of neighbouring modes contribute very similarly at their respective resonance frequencies, the fountain pattern remains robust for a large range of λ. At high frequencies, the product of neighbouring-mode amplitudes is too small to overcome the, always present, effect of wall-induced streaming, which contributes a second, antifountain (counter-rotating) vortex system to the flow. These predictions are borne out by experimental results. Exceedingly weak at low frequencies, the antifountain flow dominates at high λ and allows for complete reversal of the flow pattern upon frequency modulation, a valuable strategy, e.g. in mixing applications (Wang *et al.* 2013*a*; Wang, Rallabandi & Hilgenfeldt 2013*b*).

Simple analytical expressions have been obtained for the dominant (far-field) flow terms in both the fountain and antifountain cases, as well as for the positions of vortex centres and separatrices in the streaming flow. With this added insight, streaming flows from individual bubbles can now be described with just a few coefficients and tailored to suit the needs of a particular experiment. Moreover, as all flows are described in the limit of small streaming Reynolds number, they can be superimposed, and the design of devices featuring multiple bubbles in varying positions as well as superimposed channel flows is feasible without extensive calculations or trial-and-error.

Acknowledgements

Appendix A. Lagrangian boundary conditions at the bubble

We show here that for arbitrary surface periodic deformations given by $\zeta(\theta)$ in (2.1), both boundary conditions for the Lagrangian stream function take a simple form. The kinematic boundary condition, after defining $F(r, \theta, t) \equiv r - R(\theta, t)$, becomes $DF/Dt = 0$, which yields, using the expansion $u = u_0 + \epsilon u_1 + O(\epsilon^2)$,

$$0 = \epsilon \left(u_0 - \zeta e^{it} \right) + \epsilon^2 \left(u_1 - \left(i\zeta e^{it} \right) \frac{\partial u_0}{\partial r} + \left(i\zeta' e^{it} \right) \frac{v_0}{r} \right) + O(\epsilon^3) \quad \text{on } r = 1. \quad \text{(A 1)}$$

Likewise, the tangential stress vanishes on $F = 0$, and can be written using components of the stress tensor $\boldsymbol{\tau}$ and the unit surface normal $\hat{\boldsymbol{n}}$ and tangent $\hat{\boldsymbol{t}}$, given by

$$\hat{\boldsymbol{n}} \equiv \frac{\boldsymbol{\nabla} F}{|\boldsymbol{\nabla} F|} = \hat{\boldsymbol{e}}_r + i\epsilon\, \zeta' e^{it} \hat{\boldsymbol{e}}_\theta + O(\epsilon^2), \quad \hat{\boldsymbol{t}} = \hat{\boldsymbol{e}}_\theta - i\epsilon\, \zeta' e^{it} \hat{\boldsymbol{e}}_r + O(\epsilon^2). \quad \text{(A 2a,b)}$$

Again expanding around $r = 1$ to $O(\epsilon^2)$, we obtain

$$0 = \epsilon \tau_{0\,r\theta} + \epsilon^2 \left(\tau_{1\,r\theta} - \left(\mathrm{i}\zeta \mathrm{e}^{\mathrm{i}t} \right) \frac{\partial \tau_{0\,r\theta}}{\partial r} + \frac{\mathrm{i}\zeta' \mathrm{e}^{\mathrm{i}t}}{r} \left(\tau_{0\,rr} - \tau_{0\,\theta\theta} \right) \right) + O(\epsilon^3) \quad \text{on } r = 1. \quad (A\,3)$$

Rewriting (A 1) and (A 3) in terms of the stream function ψ, the $O(\epsilon)$ terms reproduce (2.4), while a time average over the $O(\epsilon^2)$ terms yields

$$\frac{1}{r} \frac{\partial \langle \psi_1 \rangle}{\partial \theta} = \frac{1}{r} \frac{\partial}{\partial \theta} \left(-\frac{\partial \psi_0}{\partial r} \int \frac{1}{r} \frac{\partial \psi_0}{\partial \theta} \mathrm{d}t \right) \quad \text{on } r = 1 \quad (A\,4)$$

for the kinematic boundary condition and

$$\left(\frac{\partial^2}{\partial r^2} - \frac{1}{r} \frac{\partial}{\partial r} - \frac{1}{r^2} \frac{\partial^2}{\partial \theta^2} \right) \langle \psi_1 \rangle = \frac{1}{r} \left\langle \frac{4}{r} \frac{\partial}{\partial r} \left(\frac{1}{r} \frac{\partial \psi_0}{\partial \theta} \right) \int \frac{\partial^2 \psi_0}{\partial \theta^2} \mathrm{d}t \right.$$

$$\left. - \frac{\partial}{\partial r} \left(\frac{\partial^2 \psi_0}{\partial r^2} - \frac{1}{r} \frac{\partial \psi_0}{\partial r} - \frac{1}{r^2} \frac{\partial^2 \psi_0}{\partial \theta^2} \right) \int \frac{\partial \psi_0}{\partial \theta} \mathrm{d}t \right\rangle \quad \text{on } r = 1 \quad (A\,5)$$

for the stress boundary condition. From the definition of the Stokes drift ψ_d (equation (2.7)), it is clear that it exactly compensates for (A 4) at the mean position of the interface. A lengthier calculation also shows that (A 5) and the stress tangential to $r = 1$ derived from ψ_d compensate exactly. This establishes the Lagrangian boundary conditions (2.8) for streaming flows in the plane driven by a circular object for any arbitrary deformation of its interface, and is thus more general than the analysis of Longuet-Higgins (1998).

REFERENCES

AHMED, D., MAO, X., JULURI, B. K. & HUANG, T. J. 2009 A fast microfluidic mixer based on acoustically driven sidewall-trapped microbubbles. *Microfluid Nanofluid* **7**, 727–731.

BROWN, W., PU, Z. & RYMDÉN, R. 1988 Size and shape of nonionic amphiphile micelles: NMR self-diffusion and static and quasi-elastic light-scattering measurements on c12e5, c12e7, and c12e8 in aqueous solution. *J. Phys. Chem.* **92** (21), 6086–6094.

DAVIDSON, B. J. & RILEY, N. 1971 Cavitation microstreaming. *J. Sound Vib.* **15**, 217–233.

DOINIKOV, A. A. & BOUAKAZ, A. 2010 Acoustic microstreaming around a gas bubble. *J. Acoust. Soc. Am.* **127** (2), 703–709.

LIGHTHILL, J. 1978 Acoustic streaming. *J. Sound Vib.* **61** (3), 391–418.

LIU, R. H., YANG, J., PINDERA, M. Z., ATHAVALE, M. & GRODZINSKI, P. 2002 Bubble-induced acoustic micromixing. *Lab on a Chip* **2** (3), 151–157.

LIU, X. & WU, J. 2009 Acoustic microstreaming around an isolated encapsulated microbubble. *J. Acoust. Soc. Am.* **125** (3), 1319–1330.

LONGUET-HIGGINS, M. S. 1953 Mass transport in water waves. *Phil. Trans. R. Soc. Lond. Ser.* A: *Math. Phys. Sci.* **245** (903), 535–581.

LONGUET-HIGGINS, M. S. 1998 Viscous streaming from an oscillating spherical bubble. *Proc. R. Soc. London. Series* A: *Math., Phys. Engng Sci.* **454** (1970), 725–742.

LUTZ, B. R., CHEN, J. & SCHWARTZ, D. T. 2006 Hydrodynamic tweezers: 1. Noncontact trapping of single cells using steady streaming microeddies. *Analy. Chem.* **78** (15), 5429–5435.

LUTZ, R. B., CHEN, J. & SCHWARTZ, D. T. 2005 Microscopic steady streaming eddies created around short cylinders in a channel: flow visualization and Stokes layer scaling. *Phys. Fluids* **17** (2), 023601.

MARMOTTANT, P. & HILGENFELDT, S. 2003 Controlled vesicle deformation and lysis by single oscillating bubbles. *Nature* **423** (6936), 153–156.

MARMOTTANT, P. & HILGENFELDT, S. 2004 A bubble-driven microfludic transport element for bioengineering. *Proc. Natl Acad. Sci. USA* **101** (26), 9523–9527.

NYBORG, W. L. 1958 Acoustic streaming near a boundary. *J. Acoust. Soc. Am.* **30** (4), 329–339.

PATEL, M. V., TOVAR, A. R. & LEE, A. P. 2012 Lateral cavity acoustic transducer as an on-chip cell/particle microfluidic switch. *Lab on a Chip* **12** (1), 139–145.

RANEY, W. P., CORELLI, J. C. & WESTERVELT, P. J. 1954 Acoustical streaming in the vicinity of a cylinder. *J. Acoust. Soc. Am.* **26**, 949–1006.

RILEY, N. 1966 On a sphere oscillating in a viscous fluid. *Q. J. Mech. Appl. Maths* **19** (4), 461–472.

RILEY, N. 1967 Oscillatory viscous flows. Review and extension. *IMA J. Appl. Maths* **3** (4), 419–434.

RILEY, N. 2001 Steady streaming. *Annu. Rev. Fluid Mech.* **33** (1), 43–65.

STEBE, K. J. & MALDARELLI, C. 1994 Remobilizing surfactant retarded fluid particle interfaces: Ii. controlling the surface mobility at interfaces of solutions containing surface active components. *J. Colloid Interface Sci.* **163** (1), 177–189.

STUART, J. T. 1966 Double boundary layers in oscillatory viscous flow. *J. Fluid Mech.* **24** (4), 673–687.

WANG, C., JALIKOP, S. V. & HILGENFELDT, S. 2011 Size-sensitive sorting of microparticles through control of flow geometry. *Appl. Phys. Lett.* **99**, 034101.

WANG, C., JALIKOP, S. V. & HILGENFELDT, S. 2012 Efficient manipulation of microparticles in bubble streaming flows. *Biomicrofluidics* **6** (1), 012801.

WANG, C., RALLABANDI, B. & HILGENFELDT, S. 2013*a* Frequency dependence and frequency control of microbubble streaming flows. *Phys. Fluids* **25**, 022002.

WANG, C., RALLABANDI, B. & HILGENFELDT, S. 2013*b*, *Optimized mixing strategies with acoustically driven microbubbles* Preprint.

WANG, Y., PAPAGEORGIOU, D. T. & MALDARELLI, C. 1999 Increased mobility of a surfactant-retarded bubble at high bulk concentrations. *J. Fluid Mech.* **390** (1), 251–270.